Design and Synthesis of New PEGylated Polydopamine-Based Nanoconstructs Bearing ROS-Responsive Linkers and a Photosensitizer for Bimodal Photothermal and Photodynamic Therapies against Cancer

Islam Zmerli, Nada Ibrahim, Paul Cressey, Stéphanie Denis, Ali Makky

Design and synthesis of new PEGylated polydopamine-based nanoconstructs bearing ROS-responsive linker and a photosensitizer for bimodal photothermal and photodynamic therapies against cancer

Islam Zmerli [a], Nada Ibrahim [a,b], Paul Cressey [a], Stéphanie Denis [a] and Ali Makky* [a]

[a] Université Paris-Saclay, CNRS, Institut Galien Paris-Saclay, 92296, Châtenay-Malabry, France

[b] IMESCIA, Faculté de Pharmacie, 92296, Châtenay-Malabry, France

* Corresponding author: ali.makky@universite-paris-saclay.fr

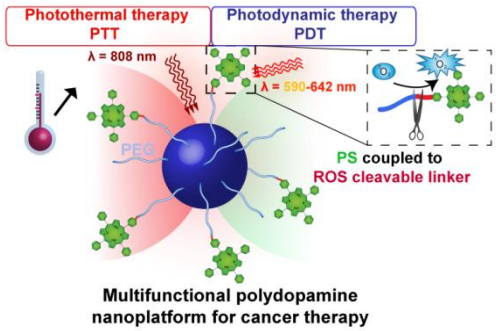

ABSTRACT

Polydopamine (PDA) nanoparticles (NPs) have recently acquired considerable attention for the development of nanoplatforms with multifunctional properties including photothermal and photodynamic activities. In addition, to their high photothermal performance, they can be easily conjugated to different types of photosensitizers (PSs) to acquire photodynamic activity. However, because of PDA free radicals scavenging properties, grafting the PSs directly to PDA surfaces may lead to inefficient photodynamic outcome. Thus, the present work aims at synthesizing and characterizing a new PEGylated polydopamine-based nanoplatform with bifunctionnal photothermal (PTT) and photodynamic (PDT) properties which allows a bimodal cancer therapy with the possibility to release the PS on demand in a spatiotemporal fashion. To do so, PDA nanoparticles with well defined size and shape were prepared by the auto-oxidative self-polymerization process of dopamine

hydrochloride in mild alkaline solution. The impact of size on the photothermal conversion efficiency was then determined. This allowed us to choose the optimal PDA nanoparticle size for photothermal applications. Next, PDA NPs were decorated with SH-PEG polymers that bear at their extremity thioketal (TK) ROS-cleavable linker coupled to trisulfonated-tetraphenylporphyrin ($TPPS_3$) was chosen as a hydrophilic photosensitizer. The grafting efficiency of the PS conjugated PEG on PDA was demonstrated *in situ* using Quartz Crystal Microbalance with Dissipation monitoring (QCM-D). In addition the photo-induced release of the PS was demonstrated by ^{1}H NMR. Finally, the PTT/PDT bimodal therapy was assessed *in vitro* on human squamous esophageal cells by illuminating the PDA NPs at two different wavelengths and showed a strong synergistic effect of combining PTT and PDT within this nanoplatform.

KEYWORDS: Polydopamine, photodynamic therapy, photothermal therapy, thioketal, ROS-responsive release.

1. INTRODUCTION

During the last few years, phototherapeutics including photodynamic therapy (PDT) and photothermal therapy (PTT) have emerged as alternative treatment modalities to tackle tumor drug resistance and conventional chemotherapy toxicity problems [1-2]. Such phototherapeutic approaches consist in the administration of photosensitizing agents (i.e., either photosensitizers or photothermal agents) that can generate upon illumination at specific wavelengths either reactive oxygen species (ROS) or heat for PDT and PTT respectively. PDT efficiency depends on the presence of oxygen in the treated tissue which limits its efficiency in the treatment of hypoxic tumors, while PTT does not require oxygen [3].

Interestingly, several recently reported studies have demonstrated that associating photothermal (PTT) and photodynamic (PDT) treatments through the combination of photothermal nanoconstructs and photodynamic agents can achieve a synergistic effect for tumor therapy [4-9]. Indeed, added to the direct cytotoxic effect of PTT, it also induces vasodilation and thus enhances the intratumoral blood flow for oxygen supply which is an essential element for the success of PDT. Thus, combining PDT and PTT in a bimodal fashion within a unique organic nanocomposite would allow synergistic effects that will enhance the therapeutic efficiencies of both treatment modalities.

However, given that the PDT efficiency is limited by the very short lifetime and the diffusion volume of singlet oxygen, controlling the release of the photosensitizer (PS) at the tumor site

has attracted tremendous attention for improving photodynamic treatment outcomes [10-11]. In fact, the controlled release of the PS at the tumor site can be achieved by linking the PS to sensitive materials that can be cleaved by (i) internal triggers found in the tumor microenvironment due to the change in the normal physiological conditions such as acidic pH, oxidative stress or enzymatic reaction but also by (ii) external energy sources such as light. Among these sensitive materials, ROS-responsive ones hold great promise for the design of nanoplatforms with the capacity to release the PS in a controlled fashion after their exposition to an external trigger such as light. ROS-responsive linkers such as, those with a thioketal (TK) group have attracted considerable attention for the release of the PS and other drugs when exposed to endogenous ROS or those generated with an external trigger [12-15]. Hence, simultaneous use of a PS with a ROS-responsive linker offers an interesting approach to provide light-triggered delivery of the PS in theoretically any site of interest.

Polydopamine (PDA) nanoparticles (NPs) also known as melanin-like NPs have recently gained high interest for the design of multifunctional nanoplatforms for cancer therapy. PDA NPs possess multiple fascinating features including simple preparation protocols, biocompatibility, simple functionalization procedures, free radicals scavenging and photothermal / photoacoustic properties [3, 16-18]. In addition, compared to other developed nanomedicines and especially those with photothermal activity based on non-organic materials such as metallic nanoparticles (Au, Pd, Ag, Fe, Cu...), PDA NPs are non-toxic, biodegradable and can be synthesized at large scale.

Several PDA-based nanosystems associated with photosensitizers with both photothermal and photodynamic functionalities have been described previously, however in all these nanoplatforms, the PSs are directly coupled to the surface of PDA nanoparticles through either physical adsorption through hydrophobic interactions or covalent bonds [3]. While physically adsorbed PSs on PDA NPs demonstrated their anticancer efficacy *in vitro* and *in vivo*, they may suffer from PS burst release following their injection into the blood circulation. Coupling the PSs to the PDA NPs via covalently bound may overcome this problem, however this is not without issues due to the ROS scavenging properties of PDA [19-20] materials because they are rich in reductive functional groups such as catechol and imine[20-23]. Thus, in the aim to tackle such problems, we propose a multifunctional smart nanosystem which allows subsequent photothermal properties and light-triggered release of the PS for controlled PDT. This nanosystem consists of a new bimodal PTT/PDT PDA-based nanoplatform which is decorated with hydrophilic PEG chains and bearing at their extremity

thioketal as ROS-cleavable linker that is bound to a PS. Trisulfonated-tetraphenylporphyrin ($TPPS_3$) was chosen as the PS due to its acceptable water solubility. The thioketal ROS-responsive linker should allow the release of the PS in a spatial, temporal, and dose-controlled fashion following the illumination of the tumor to exert their photodynamic activity on a selected tissue depending on the releasing site of the PS. Added to the anti-fouling properties of the PEG chains against proteins enabling longer blood circulation times, they play the role of the spacer between the PDA NPs and the photosensitizers. These NPs can be used for the treatment of tumors that do not require near infrared absorbing PSs and can be accessed by light without any surgical operation such as esophageal cancer. Upon appropriate light excitation of the PS, the ROS/$^1O_2$ generated *in-situ via* the photodynamic process would serve as a trigger leading to the delivery of the PS and the photodynamic activity in a spatiotemporally and dose-controlled manner. Non-ROS responsive PDA-based NPs were also prepared and served as control.

In previous work, we established tightly controlled experimental conditions to synthesize and PEGylate PDA NPs with well-defined and reproducible physicochemical properties including size, yield and nanomechanical properties [3, 16]. Herein, we examined quantitatively for the first time the impact of PDA NPs size on their photothermal conversion efficiency. Afterwards, we described the functionalization steps adopted for the development of the bimodal PTT/PDT PDA-based nanoplatform proposed in this work. Finally, as proof of concept, the bimodal therapy PTT/PDT efficiency of these nanosystems was assessed *in vitro* on human esophageal squamous cell lines.

2. MATERIALS AND METHODS

2.1. Chemicals

2,2'-(propane-2,2-diylbis(sulfanediyl)diethanamine (thioketal linker (TK), M_w = 194.38 g/mol, d = 1.083 g/ml) was obtained from Fluorochem (Derbyshire, United Kingdom), dopamine hydrochloride (DA, 98%, M_w = 189.64 g/mol), fluorescein isothiocyanate isomer I (FITC, ≥ 99%, M_w = 389.38 g/mol), thionyl chloride ($SOCl_2$, ≥ 99%, M_w = 118.97 g/mol, d = 1.64 g/ml), poly(ethylene glycol) 2-mercaptoethyl ether acetic acid (SH-PEG_{2000}-COOH, n = 45, M_n = 2100 g/mol), tris(2-caroxyethyl)phosphine hydrochloride (TCEP, M_w = 286.65 g/mol), Sodium iodide (NaI, ≥ 99%, M_w = 149.89 g/mol), tris(hydroxymethyl)aminomethane (Tris buffer, ≥ 99.8%, M_w = 121.14 g/mol), and anhydrous pyridine were purchased from Sigma Aldrich (St. Louis, MO, United States), hydrogen peroxide (H_2O_2, 30% (w/w)) and

ammonium hydroxide (25% NH_3) from Merck (Germany), 5-(4-carboxypropylcarbamoylphenyl)-10,15,20-(tri-4-sulfonatophenyl)porphyrin triammonium ($TPPS_3$-COOH, > 95%, M_w = 1034.24 g/mol), 5-(4-aminophenyl)-10,15,20-(tri-4-sulfonatophenyl)porphyrin triammonium ($TPPS_3$-NH_2, > 95%, M_w = 921.03 g/mol) and 5-(4-carboxypropylcarbamoylphenyl)-10,15,20-(tri-4-sulfonatophenyl)porphyrin triammonium 2,2'-(propane-2,2-diylbis(sulfanediyl)diethanamine conjugate ($TPPS_3$-TK-NH_2, M_w = 1211.35 g/mol) were provided by PorphyChem (Dijon, France), $CDCl_3$ and DMSO-d_6 were provided from Eurisotop (Saint-Aubin, France), HPLC-grade methanol (MeOH) and pyridine were purchased from VWR Chemicals (Radnor, PA, USA), Fetal bovine serum (FBS) was provided from Gibco (Invitrogen, Carlsbad, California, United States), 1 kDa dialysis membrane was purchased from Spectrum labs (California, United States), Ultrapure water was produced by a Millipore MilliQ Direct 8 water purification system with a resistivity of 18.2 MΩ cm at 25 °C.

2.2. Synthesis of polydopamine nanoparticles

The PDA NPs were synthesized following the same procedure detailed in our previous work [16]. In brief, ultrapure water was mixed with ethanol (70/30 % v/v) and an aqueous solution of ammonia (25% NH_3). Dopamine hydrochloride was pre-dissolved in water and added to the aforementioned mixture under mild stirring for 24 hours at 25°C. The final concentration of dopamine was 3.2 mg/ml. The NPs were purified by centrifugal filtration in 30 kDa MWCO Amicon filters and subsequently washed with water three times (3 x 10 ml). Centrifugations were carried out at ~2000 g, 4°C for 20 min using SL-200 RFID rotor (NuAir Awel, UK). The volumes retained were redispersed in either ultrapure water or Tris buffer and then stored at 4°C.

To study the impact of the NPs size on their photothermal efficiency, different molar ratios of ammonia/dopamine (10, 20, 25 and 30) were used while maintaining the dopamine concentration unchanged. All PDA NPs formulations were reproduced three times.

2.3. Study of the photothermal conversion efficiency of PDA NPs in solution

1 ml of PDA NPs suspension at different concentrations ranging from 50µg/ml to 400µg/ml, in Tris buffer (10mM, pH= 7.4) was loaded in a quartz cell and placed 1 cm away from the laser diode. The suspension was then illuminated by the means of a laser diode module equipped with a laser diode driver and a temperature controller (LDM90, LDC220C, TED200C from Thorlabs Inc. Newton, New Jersey, United States) at a wavelength of 808 nm and an output power of 250 mW, 500 mW, 750 mW or 1000 mW. At 1000 mW power, the fluence at this distance was estimated using an optical power meter (PM160T Optical Power Meter, from Thorlabs Inc. Newton, New Jersey, United States) to be 2 W/cm^2. The temperature increase inside the suspension upon illumination was recorded using two K-type thermocouples that were placed in two opposite corners of the quartz cell while a small magnetic stirrer is placed inside to get a uniform temperature (**Figure S1).**

The process of nanoparticles-mediated photothermal hyperthermia can be described as a collective heating model [24]. The calculation of the photothermal conversion efficiency (η) can be calculated following the same method already described by Roper *et al.* [25] and reproduced by many other authors [17, 26-30]. The full description of the calculation method we adopted in this work is detailed in the **supporting information section** and **Figure S2**.

2.4. Evaluation of the photo-induced degradation of ROS-cleavable linkers

In the case of thioketal, acetone would be produced following the ROS-sensitive bond rupture [12, 31], which could be monitored by ^{1}H NMR. The cleavage of the thioketal group under illumination was assessed as follows: The $TPPS_3$-TK-NH_2 conjugate was dissolved in DMSO-d_6 at a concentration of 70 mM, in presence of 70 mM 1,3,5-trimethoxybenzene (TMB) used as an internal standard. The solution mixture was placed in a 3 mm NMR tube and illuminated at different time intervals using a 642 nm diode laser (Thorlabs Inc. Newton, New Jersey, United States) at 200 $mW.cm^{-2}$. ^{1}H NMR (400 MHz) spectrum was recorded after each illumination and signals intensity of the characteristic peak of thioketal (-C$C\underline{H_3}$, δ = 1.59 ppm) and of the potentially formed acetone (δ = 2.09 ppm) was integrated relatively to those of TMB, which allowed us to study the degradation kinetics of the thioketal linker.

2.5. Synthesis of $TPPS_3$-conjugated PEG polymers

In order to prepare ROS-responsive and non-ROS responsive PDA-based nanoparticles, first we synthesized two different $TPPS_3$-conjugated PEG polymers through covalent binding of either $TPPS_3$-TK-NH_2 or $TPPS_3$-NH_2 to SH-PEG-COOH, respectively.

The synthetic procedure the $TPPS_3$-conjugated PEG polymers can be summarized as follows:

2.5.1. Dimerization of SH-PEG_{2000}-COOH chains

This step aims at blocking the thiol groups of the polymer to avoid its intra- or inter-molecular interactions with the carboxylic group of PEG chains. For that, SH-PEG_{2000}-COOH (100 mg, 47.6 µmol, 1 equiv.) was dissolved in deionized water (5 ml), 0.5 ml of a 10 mM NaI solution (0.1 equiv.) and 60 µl of a 3% H_2O_2 (1.1 equiv.) were added and the mixture was incubated overnight at room temperature. The reaction crude was dialyzed in deionized water through a 1 kDa dialysis membrane. The separated product (white powder, yield = 91%) was characterized using ^{1}H NMR ($CDCl_3$, 300 MHz) in comparison to SH-PEG_{2000}-COOH (**Figure S3 A-B**). Although the integration of the signals, for both products, did not lead to a correct number of protons between the broad signal of ethylene glycol pattern and the signals of the terminal chains, the successful dimerization of PEG was evidenced by the following elements: (i) the absence of the signal at δ = 1.59 ppm present in the spectrum of the SH-PEG_{2000}-COOH and corresponding to the -S*H* group, (ii) the shift in the signal corresponding to -*C*H_2-SH, from δ = 2.73-2.66 ppm to δ = 2.90-2.86 ppm for SH-PEG_{2000}-COOH and COOH-PEG_{2000}-S-S-PEG_{2000}-COOH respectively, due to the changes in the chemical environment after disulfide formation, and (iii) the difference in the marginal peaks of the broad signal at δ = 4.06-3.38 ppm and δ = 4.03-3.32 ppm for SH-PEG_{2000}-COOH and COOH-PEG_{2000}-S-S-PEG_{2000}-COOH respectively, due to differences in the coupling of the terminal chains protons.

2.5.2. Acyl chloride formation

The carboxylic acid functions of the dimerized PEG chains (90 mg, 21.4 µmol) were activated in pure anhydrous $SOCl_2$ (2 ml) under inert atmosphere ($Ar_{(g)}$) and ambient temperature, to form acyl chloride moieties. The reaction mixture was stirred for 3 h and the solvent was then carefully evaporated. Due its high sensitivity, the product obtained was directly engaged in the next step with no further characterization.

2.5.3. Coupling of the activated PEG chains to the $TPPS_3$-TK-NH_2 or $TPPS_3$-NH_2

$TPPS_3$-TK-NH_2 or $TPPS_3$-NH_2 (13 mg or 9.9 mg respectively, 10.7 µmol, 1 equiv.) were added to the $SOCl_2$-activated PEG dimer (90 mg, 21.4 µmol, 2 equiv.) and dissolved in anhydrous pyridine. The mixture was heated at 115 °C under reflux and stirred overnight under $Ar_{(g)}$. Pyridine was then removed under vacuum and the crude was purified using preparative TLC with Methanol/Water/Pyridine 70/30/0.2% as eluant. The products ($TPPS_3$-TK-NH-PEG-S)$_2$ (yield 55%) and ($TPPS_3$-NH-PEG-S)$_2$ (yield 50%) were isolated as dark purple-brown solids. The dimmers were then reduced using TCEP in Tris buffer (10 mM, pH 8.5) in order to regenerate the thiol group on the extremity of PEG chains, crucial for their conjugation to the surface of PDA NPs. The products obtained were dialyzed against deionized water using a 1 kDa dialysis membrane and characterized by ^{1}H NMR (DMSO-d_6, 400 MHz) (**Figure S4 A-B**). For $TPPS_3$-TK-PEG_{2000}-SH conjugate: δ (ppm) 9.04, 8.78, 8.64, 8.17, 8.02, 7.84, 7.35, 7.23, 6.85 and 6.68 (Aromatic protons of $TPPS_3$-TK-NH_2), 5.33, 5.09, 4.80, 2.68-2.67, 2.37, 2.33, 2.18, 2.11, 1.98 and 1.61 (Aliphatic protons of $TPPS_3$-TK-NH_2), 3.93-3.40 and 2.91-2.88 (protons of PEG chains). For $TPPS_3$-NH-PEG_{2000}-SH conjugate: δ (ppm) 9.02-9.01, 8.85, 8.65-8.61, 8.18-8.15, 8.07, 7.79, 7.19, 7.13, 6.96 and 6.84 (Aromatic protons of $TPPS_3$-NH_2), 3.85-3.42 and 2,72-2.68 (protons of PEG chains). In fact, due to the limited quantity of products available for analysis, the NMR spectra of the synthesized Porphyrin-PEG conjugates were not well-resolved. The presence of the intense broad signal related to PEG chains renders the interpretation of the other peaks more difficult. A detailed peaks attribution could not hence be performed. However, by referring to the NMR spectra of free $TPPS_3$-(TK)-NH_2 and SH-PEG_{2000}-COOH in DMSO-d_6, we could clearly distinguish the presence of the characteristic peaks of the porphyrin which are present in the region of δ comprised between 9.04 – 6.68 ppm and relative to the pyrrole and the phenyl groups, together with the broad peak relative to the ethylene glycol pattern of PEG centered at δ 3.51 ppm. The presence of peaks in the range of δ comprised between 3.20 and 1.10 ppm is attributed to the protons present on the aliphatic chain of $TPPS_3$-TK-NH_2 and PEG terminal chains for the $TPPS_3$-TK-PEG_{2000}-SH conjugate and of the PEG terminal chains for the $TPPS_3$-NH-PEG_{2000}-SH.

2.6. Evaluation of the $TPPS_3$-TK-PEG_{2000}-SH grafting efficiency on PDA film using Quartz Crystal Microbalance with Dissipation monitoring (QCM-D)

The ability of the synthesized polymeric conjugates to be efficiently grafted on a PDA surface was verified *in situ* on planar geometry using QCM-D. This experiment was performed at 25 °C using QCM-D-E4 (Q-Sense, Gothenburg, Sweden) as previously described[16]. In brief, the SiO_2-coated quartz sensor was sonicated in SDS 10% for 5 minutes, rinsed thoroughly with ultrapure water and dried under nitrogen, then treated with UV/Ozone for 40 minutes. QCM-D channels were also cleaned prior to use, using Hellmanex solution at 2% (% m/m). Frequency and dissipation shifts (Δf and ΔD) were monitored for the overtones n = 3, 5, 7, 9 and 11. First, a PDA film was formed on the SiO_2-coated quartz sensor by injecting a 2 mg/ml dopamine solution in Tris buffer (10 mM, pH 8.5) at 250 µl/min, until the frequency shifts reached the values fixed previously in order to obtain a similar layer thickness (Δf_5 ~ -100 Hz, reached after ~ 2 h). After rinsing and buffer switch, a 1.55 mg/ml solution of $TPPS_3$-thioketal-PEG_{2000}-SH was injected in Tris buffer (10 mM, 150 mM NaCl, pH 8.5) as optimized previously [16]. Δf and ΔD were monitored until saturation was reached and an excessive rinsing was performed at the end of the experiment in order to remove the loosely grafted chains.

2.7. Preparation and characterization of PTT/PDT bimodal PDA-based NPs

A mixture of COOH-PEG_{2000}-SH and $TPPS_3$-(TK)-PEG_{2000}-SH at an equal molar ratio was used to functionalize bare PDA NPs of ~130 nm in Tris buffer (10 mM, 150 mM NaCl, pH 8.5). The final concentrations were 1 mg/ml for PDA NPs, 5 mg/ml for COOH-PEG_{2000}-SH, and 7.8 mg/ml or 7.1 mg/ml for $TPPS_3$-TK-PEG_{2000}-SH or $TPPS_3$-NH-PEG_{2000}-SH, respectively. The mixtures were incubated for 24 h under mild stirring at 25 °C. The NPs were then purified by centrifugal filtration in Amicon tubes (MWCO 50 kDa) using a SL-200 RFID rotor (NuAir Awel, UK) at ~2000 g and thoroughly washed until the supernatants became clear.

The synthesized nanoparticles were characterized in terms of hydrodynamic diameter, zeta potential and absorbance spectrophotometry for the quantification of the $TPPS_3$ grafting efficiency.

2.7.1. Dynamic light scattering (DLS) and zeta potential measurements

The size distribution and surface charge of PDA NPs before and after functionalization were determined using a Zetasizer (Nano-ZS 90, Malvern Instruments, UK) with a detection angle

of 90 °. NPs were dispersed in Tris buffer (10 mM, pH 7.4) and zeta potential was measured in presence of low ionic strength (5 mM NaCl). All measurements were carried out in triplicates at 25 °C.

2.7.2. UV-visible absorbance and Quantification of $TPPS_3$ conjugated to PDA NPs

The UV-visible-NIR absorbance of PDA NPs functionalized with $TPPS_3$-TK-PEG_{2000}-SH or $TPPS_3$-NH-PEG_{2000}-SH was measured in Tris buffer (10 mM, pH 8.5) using a Cary 300 Bio UV-vis spectrophotometer (Varian, USA). The content of $TPPS_3$-TK-NH_2 or $TPPS_3$-NH_2 conjugated to NPs surface was estimated by measuring the PS absorbance at a specific wavelength (λ= 414 nm) using a CARY 100 Bio UV–visible spectrophotometer (Varian, USA). By comparison with standards at specific concentrations (**Figure S5**), the PS coupling efficiency was determined on normalized absorbance spectra of PDA formulations. This was done by subtracting the absorbance of non-functionalized NPs from that of PS-conjugated NPs measured at a similar PDA concentration. The molecular ratio PS/NPs was then calculated using equation 1.

$$PS/NPs = \frac{[PS]_{molecular}}{[PDA\ NPs]_{molecular}} \qquad \text{(eq 1)}$$

Where $[PS]_{molecular}$ is the molecular concentration (in molecules.l^{-1}) of $TPPS_3$-TK-NH_2 or $TPPS_3$-NH_2 deduced from the absorption measurements and $[PDA\ NPs]_{molecular}$ is the molecular concentration (in molecules.l^{-1}) of PDA NPs calculated as follows:

$$[PDA\ NPs]_{molecular} = \frac{[PDA\ NPs]_{weig\square t}}{V_{PDA\ NPs} \cdot \rho_{PDA}} \qquad \text{(eq 2)}$$

Where $[PDA\ NPs]_{weight}$ is the weight concentration of PDA NPs, $V_{PDA\ NPs}$ is the average volume of PDA NPs calculated based on DLS measurements of their hydrodynamic diameter and ρ_{PDA} the density of PDA which is equal to 1981 ± 74 kg/m^3 as determined previously[16].

2.8. Cell culture experiments

Two cell lines were used to evaluate the cytotoxicity and phototoxicity of nanoparticles and free molecules: (i) HET-1A, a human esophageal squamous cell line used as a model for healthy esophageal epithelium and purchased from the American Type Culture Collection (Manassas, VA), and (ii) KYSE-30, squamous esophageal carcinoma cells, purchased from Sigma Aldrich. HET-1A and KYSE-30 cells were cultured in Roswell Park Memorial Institute 1640 (RPMI 1640) medium supplemented with 10% FBS and antibiotics (100 IU/ml penicillin – 100 µg/ml streptomycin) in a humified incubator at 37 °C with a 5% CO_2

atmosphere. Cells were passaged every three days at a confluence of 70-80% using 0.25% trypsin / ethylenediaminetetraacetic acid (EDTA).

2.8.1. *In vitro* cellular uptake assessment by flow cytometry

The cellular uptake of PDA NPs, PDA-PEG NPs and free $TPPS_3$-COOH was measured on HET-1A and KYSE-30 in order to determine the incubation time needed for an efficient cellular internalization for the next phototoxicity assays. PDA nanoparticles were labeled with a fluorescent dye, FITC, prior to their incubation with cells, non-labeled nanoparticles were used as a control.

HET-1A and KYSE-30 cells were seeded for 24 h in 12-well culture plates (500 µl, at 6×10^4 and 1×10^4 cells per well respectively). Then, 500 µl of PDA or PDA-PEG NPs or $TPPS_3$-COOH in culture medium were then added to each well at a final concentration of 100 µg/ml and 20 µM for PDA-based NPs and free PS, respectively. The plates were further incubated at 37 °C for 30 min, 1 h, 2 h, 6 h, or 24 h and the cells were then washed twice with PBS, detached using trypsin/EDTA, centrifuged at 200 g after dilution in cell culture medium and re-dispersed in PBS. The cellular uptake was then examined using an Accuri C6 Plus flow cytometer (BD Biosciences, USA). 10000 events were counted for each sample and fluorescence intensity was measured with the FL1 (λ_{exc} = 488 nm) and FL4 (λ_{exc} = 640 nm) channels for the PDA/PDA-PEG NPs and for the $TPPS_3$-COOH respectively.

2.8.2. *In vitro* evaluation of the cytotoxicity at dark and the phototoxicity

The cytotoxicity of PDA and PDA-PEG NPs was studied at final concentrations ranging from 10 to 500 µg/ml at 24, 48 and 72 h. The phototoxicity of free $TPPS_3$ was assessed at 24, 48 and 72 h using concentrations reaching 60 µM and after NIR irradiation for 14 min at 2 $J.cm^{-2}$ using the orange light (PDT), the toxicity in the dark of these samples was evaluated in parallel. For the full PDA-PEG-PS NPs, final concentrations ranging from 10 to 200 µg/ml of PDA were tested. Their cytotoxicity was evaluated in the dark and their phototoxicity after 72 h was assessed after illuminations using either the 808 nm laser at an irradiance of 2 $W.cm^{-2}$ for 10 min (PTT), or the orange filtered lamp at a 2 $J.cm^{-2}$ fluence (PDT), or the combination of both irradiation procedures (PTT/PDT). Temperature changes obtained after PTT irradiation and infrared images of these illuminated samples were recorded using a FLUKE Ti401 PRO thermal camera (Fluke Corporation, Washington, United States).

Cells were seeded in a 96-well plate at a density of 12×10^3 and 2×10^3 cells per well for HET-1A and KYSE-30, respectively (100 µl per well) and incubated for 24 h. Then, 100 µl of

culture medium containing PDA NPs, PDA-PEG NPs, PDA-PEG-PS NPs or free PS were added, in the dark, to the wells at different concentrations and incubated for an additional 24 h. Cells incubated with total 200 µl of culture medium alone served as untreated control. The following day, the culture medium was aspirated and replaced, to remove non-internalized products. Cells were either further incubated in dark for the evaluation of their cytotoxicity or illuminated as previously described for the assessment of their phototoxicity. The cell viability was determined using the MTT test after 24, 48 and 72 h. In brief, 20 µl of sterile MTT solution were added to each well (final concentration 0.5 mg/ml) and the cells were further incubated for 1 h (37 °C, 5% CO_2). Then, the medium was removed and 200 µl of DMSO was added to the wells in order to dissolve the formazan produced by MTT metabolization in the alive cells. After 10 min shaking, the optical density (OD) was measured at 570 nm using an ELISA plate reader (Labsystems Multiskan MS, France). Experiments were performed in triplicate.

For PDA-related experiments, the OD was measured at 650 nm and 570 nm and the OD of formazan at 570 nm was estimated following the protocol described by Nieto *et al.* [32], in order to avoid the interference of PDA absorption at 570 nm.

2.8.3. Analysis of synergistic activity of $TPPS_3$-conjugated PDA-PEG NPs

In order to quantitatively analyze the type of interactions between the $TPPS_3$ photosensitizing molecule and PDA NPs, the combination index (CI) was calculated using CompuSyn® software (version 1.0, CompuSyn Inc., United States., www.combosyn.com) based on the Chou-Talalay method [33-34] (Equation 3).

$$\mathrm{CI} = \frac{[EI]_1'}{[EI]_1} + \frac{[EI]_2'}{[EI]_2} \qquad \text{(eq 3)}$$

The $[EI]_i$ and $[EI]_i$' correspond to the concentrations of the associated drugs used separately or in combination, respectively, leading to a similar inhibitory effect. A CI value > 1 indicates an antagonism, CI = 1 corresponds to additive effects, and CI < 1 indicates synergism between the associated drugs. In this study, the inhibitory effect designated as the faction affected (Fa) corresponds to the cell killing effect and was calculated using the following equation (Equation 4)

$$\mathrm{Fa} = 1 - \frac{\%\ cell\ viability}{100} \qquad \text{(eq 4)}$$

3. RESULTS AND DISCUSSION

3.1. Neat PDA nanoparticles preparation and evaluation of their photothermal conversion efficiency in buffer

Before preparing the bimodal PDA nanosystems decorated with PEG chains and bearing at their extremity the ROS-responsive linker and $TPPS_3$ PS, we wanted to evaluate the photothermal conversion efficiencies of PDA NPs and the impact of their size on such aspect. Thus, PDA NPs with different sizes have been synthesized following the oxidization of dopamine in alkaline conditions in ultrapure water/ethanol (70/30% v/v) in the presence of ammonia (25% NH_3) at different [Ammonia]/[Dopamine] ratio as described previously [35]. After the purification of PDA NPs with centrifugal filtration, they were illuminated with a laser diode in different experimental conditions in order to evaluate their photothermal conversion efficiency. Indeed, Liu *et al.* [17] have first demonstrated the ability of PDA nanoparticles to convert light into heat with a conversion efficiency of ~ 40% for nanoparticles with hydrodynamic diameter of ~ 70 nm [17]. However, PDA NPs may have different shapes, packing densities of oligomers or even different chemical functionalities at their surface [36-38]. This may lead to different photothermal properties than those already described in the literature. Thus, in order to assess the photothermal behavior of PDA NPs, we have started the evaluation of photothermal efficiency with PDA NPs of 125 nm of hydrodynamic diameter (D_H) which were prepared following the same procedure (Ratio [Ammonia]/[Dopamine] = 25) described previously [16]. In fact, nanoparticles with a diameter less than 200 nm are usually used for *in vivo* applications due to their better pharmacokinetics properties and their passive accumulation in tumors *via* the enhanced permeability and retention (EPR) effect [39-40]. Hence, suspensions of PDA NPs were illuminated with a laser diode at a wavelength of 808 nm and an irradiance of 2 $W.cm^{-2}$ until a steady state of temperature is reached. Afterwards the laser was turned off, and the suspensions were allowed to cool back to the ambient temperature. A typical temperature profile versus time of PDA NPs is shown in **Figure 1A**.

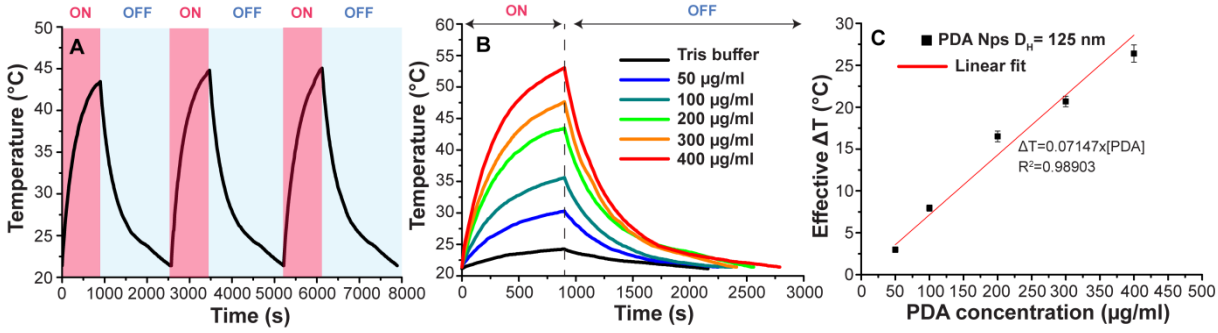

Figure 1. (A) Plot of temperature profile versus time registered under NIR irradiation (808 nm laser at 2 $W.cm^{-2}$) of a 200 µg/ml PDA NPs suspension (D_H = 125 nm) for 900 s, followed by a cooling phase (laser turned off). The cycle laser On-Off was repeated three times to assess NPs photostability. (**B)** Temperature increase of a Tris buffer solution and PDA NPs suspensions (D_H = 125 nm) at different concentrations as a function of NIR illumination time (808 nm, 2 $W.cm^{-2}$). **(C)** Temperature changes (ΔT) registered after 900 s of NIR illumination as a function of PDA NPs concentration.

As depicted in **Figure 1A**, the temperature of the PDA NPs suspension increased exponentially upon laser illumination until reaching a steady state temperature (ΔT = 20.8 ± 0.4 °C) after 900 s followed by over 1000 s of cooling. The NPs suspensions were then subjected to two consecutive laser illuminations. The heating cycles are fully reproducible indicating the photothermal stability of PDA nanoparticles as already demonstrated by Liu *et al.* [17]. Next, we wanted to determine the maximal reachable effective temperature increase as a function of NPs concentration. As shown in **Figure 1B**, compared to Tris buffer, PDA NPs suspensions exhibited much higher temperature increase of 9.5-33°C in the concentration range of 50 µg/ml to 400 µg/ml. This behavior demonstrates that the photothermal conversion effect is an intrinsic property of PDA NPs [17]. In addition, as the concentration increases, the number of nanoparticles increases and the collective heat generated by the nanoparticles induced a proportional increase of the effective ΔT as shown in **Figure 1C**. The temperature changes can be thus fitted linearly as function of PDA concentrations. However, it should be noted that suspensions containing high NPs concentration exhibit larger attenuation factor for light which induces a lower penetration depth and thus non homogenous heat distribution because not all of nanoparticles will receive the same light intensity. This is a very important aspect that should be taken into account for *in vivo* applications to ensure that the inner part of the tumor is homogenously and sufficiently heated [41]. In our experiments, all of the NPs suspensions were illuminated during a continuous stirring which allows homogenous light illumination and heat distribution inside the suspension volume. Additionally, the impact of laser power was also investigated on the photothermal behavior of PDA NPs. As shown in **Figure 2A**, the higher the laser intensity, the higher the temperature increment is obtained. Moreover, the plotted effective ΔT (**Figure 2B**) increased linearly as function of the laser power between 250 mW and 1000 mW (0.5 $W.cm^{-2}$ to 2$W.cm^{-2}$). This indicates that the photothermal behavior of PDA nanoparticles can be tuned efficiently with the laser power up to 1000 mW to get the desired temperature without losing their photothermal conversion

properties as in the case of gold nanomaterials that melt at high laser intensity or exposure time thus leading to photothermal instability [42-44].

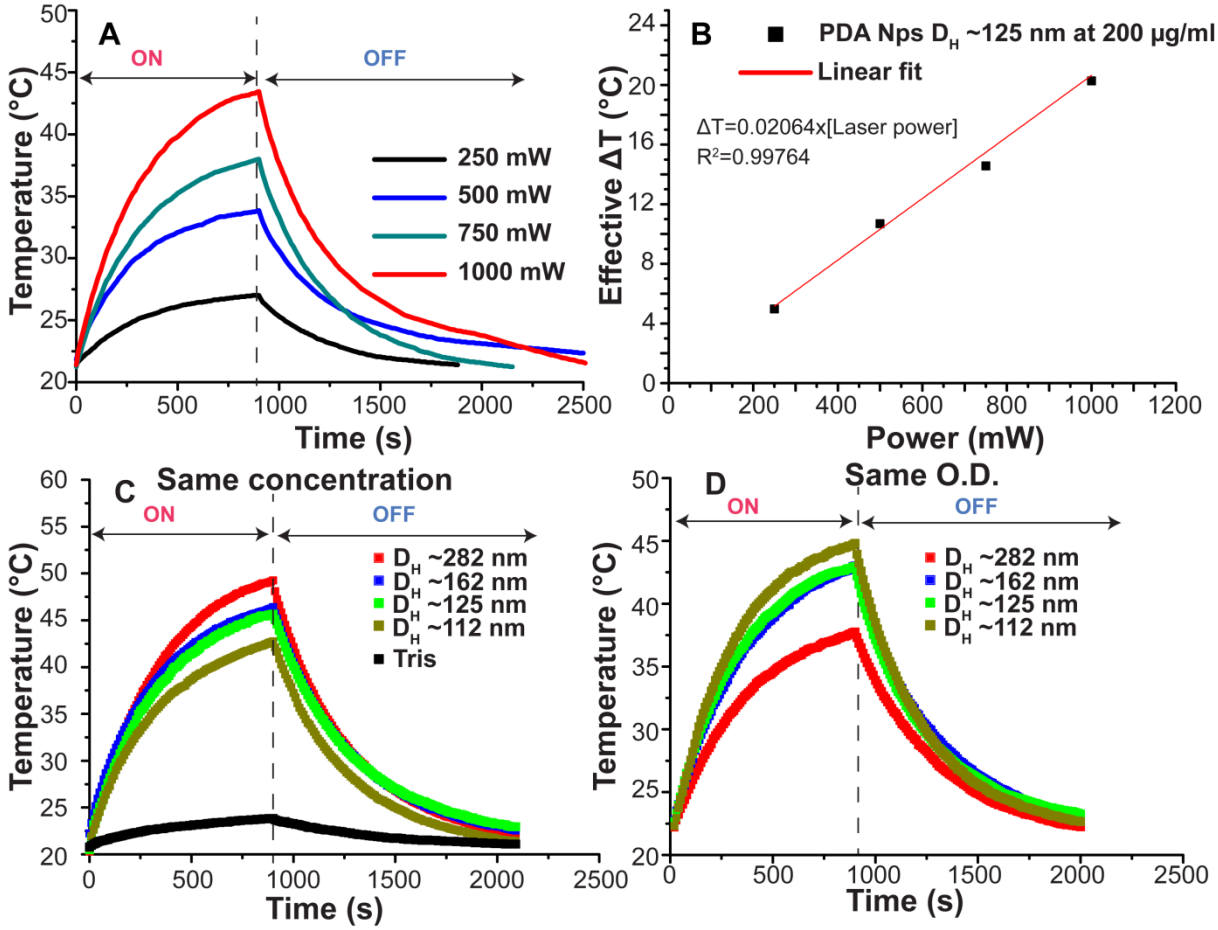

Figure 2. (A) Temperature profile versus time registered during a thermal heat cycle of a 200 µg/ml PDA NPs suspension (D_H = 125 nm) illuminated using an 808 nm laser diode at different laser powers. **(B)** Temperature changes (ΔT) registered after 900 s of NIR irradiation of a 200 µg/ml PDA NPs suspension (D_H = 125 nm) as a function of laser power. **(C)** Temperature changes profile registered during a thermal heat cycle of 200 µg/ml PDA NPs suspensions with different hydrodynamic diameters and illuminated using a 808 nm laser diode at 2 W.cm^{-2}. **(D)** Temperature changes profile registered during a thermal heat cycle of PDA NPs with different hydrodynamic diameters, whose optical densities (O.D.) were calibrated at 0.25, and illuminated using an 808 nm laser diode at 2 W.cm^{-2}.

Next, the cooling phases of the thermal cycles following the illumination of PDA nanoparticles suspensions were analyzed to determine the rate of heat transfer ($1/\tau_s$) from the system to the environment as described above. An average value of 367.2 ± 19.4 s for τ_s was obtained and used for the photothermal conversion efficiencies calculation. For PDA NPs with an average hydrodynamic diameter of 125 nm, the photothermal conversion efficiency was 46.2 ± 1.1 % which is in line with other reported values in the literature [17, 30].

Having studied the photothermal properties of nanoparticles with an average diameter of ~ 125 nm, we wanted to assess the impact of NPs size on their photothermal conversion efficiencies. In fact, when the size of spherical nanoparticles is modified, their scattering and absorption cross sections will also be modified which may in turn change their photothermal conversion efficiency. In other words, when the light hits the nanoparticles, they can simultaneously scatter and absorb light. The sum of both absorption and scattering constitutes the extinction ($Q_{ext} = Q_{abs} + Q_{scatt}$). Thus, in order to study this aspect, PDA nanoparticles with different diameters at a concentration of 200 µg/ml in Tris buffer were illuminated at a laser irradiance of 2 $W.cm^{-2}$. As depicted in **Figure 2C**, the larger the PDA nanoparticles diameter, the higher the increase in temperature. Using these data, we have calculated their conversion efficiencies. As shown in **Table 1 and Figure S6**, whereas the effective ΔT increases with their size, the photothermal conversion efficiency is reduced. This could be explained by the Mie's theory [45-46] which indicates that larger nanoparticles exhibit more scattering than absorption. Thus, a large fraction of light will be scattered compared to that absorbed by the NPs which reduce their photothermal conversion efficiency. Additionally, it should be noted that although the PDA concentration was kept constant for all these measurements, the number of PDA NPs with larger diameter is however less compared to that with smaller ones. This effect would counterpart the collective photothermal conversion efficiency.

Table 1. The impact of PDA NPs hydrodynamic diameter on their optical densities and photothermal conversion properties. The reported values are the average ± standard deviation of n = 3.

Hydrodynamic diameter (nm)	**Optical density at 808 nm (a. u.)**	**ΔT effective (°C)**	**Photothermal conversion efficiency (%)**
282±2	0.72	25.6 ± 0.4	31.6 ± 0.4
162±5	0.31	21.3 ± 0.6	42.1 ± 1.4
125±3	0.25	20.8 ± 0.4	46.2 ± 1.1
112±3	0.24	18.8 ± 0.4	43.4 ± 1.4

In order to demonstrate our thoughts, PDA NPs at different sizes but at the same optical density (O.D. = 0.25) were illuminated using the same experimental setup. As depicted in **Figure 2D**, PDA NPs with larger size revealed lower temperature increase than smaller one, thus demonstrating that smaller PDA NPs convert light to heat more efficiently than larger

one due to their higher absorption/extinction ratio. Similar tendency has been also observed by other authors for other gold nanoparticles [26] and Cu^{2+} laded PDA NPs [30].

3.2. Choice of the PS and Study of the thioketal cleavage under $TPPS_3$ light irradiation

Since the PS is to be grafted on the extremity of the PEG, it should have hydrophilic character to prevent unwanted aggregation. For this purpose, a trisulfonated tetraphenylporphyrin ($TPPS_3$) was selected, as it is commercially available in the carboxylic and amino forms, needed for the preparation of ROS-responsive and non-responsive nanosystems, respectively. $TPPS_3$-COOH coupled to the amine-terminated thioketal linker could also be directly provided from PorphyChem®.

Before preparing the bimodal PTT/PDT PDA NPs and evaluating their phototoxic efficiency *in vitro*, we wanted to assess the feasibility of light-triggered thioketal cleavage upon $TPPS_3$ illumination by using ^1H NMR (400 MHz, in DMSO-d_6) as well as its kinetics. To this aim, the $TPPS_3$-TK-NH_2 compound was dissolved at a concentration of 70 mM in deuterated DMSO, and the solution was illuminated with a 642 nm laser diode at 100 mW (200 $mW.cm^{-2}$) with different illumination durations. As shown in the **Figure 3**, upon the illumination of the NMR tube containing the $TPPS_3$-TK-NH_2, the corresponding peak of the TK (δ = 1.59 ppm) starts to decrease with subsequent increase of the acetone peak (δ = 2.09 ppm). This demonstrates that the TK linker is decomposed upon the PS illumination due to the generation of ROS. The decomposition of thioketal group was further quantified as function of illumination duration using TMB as internal reference.

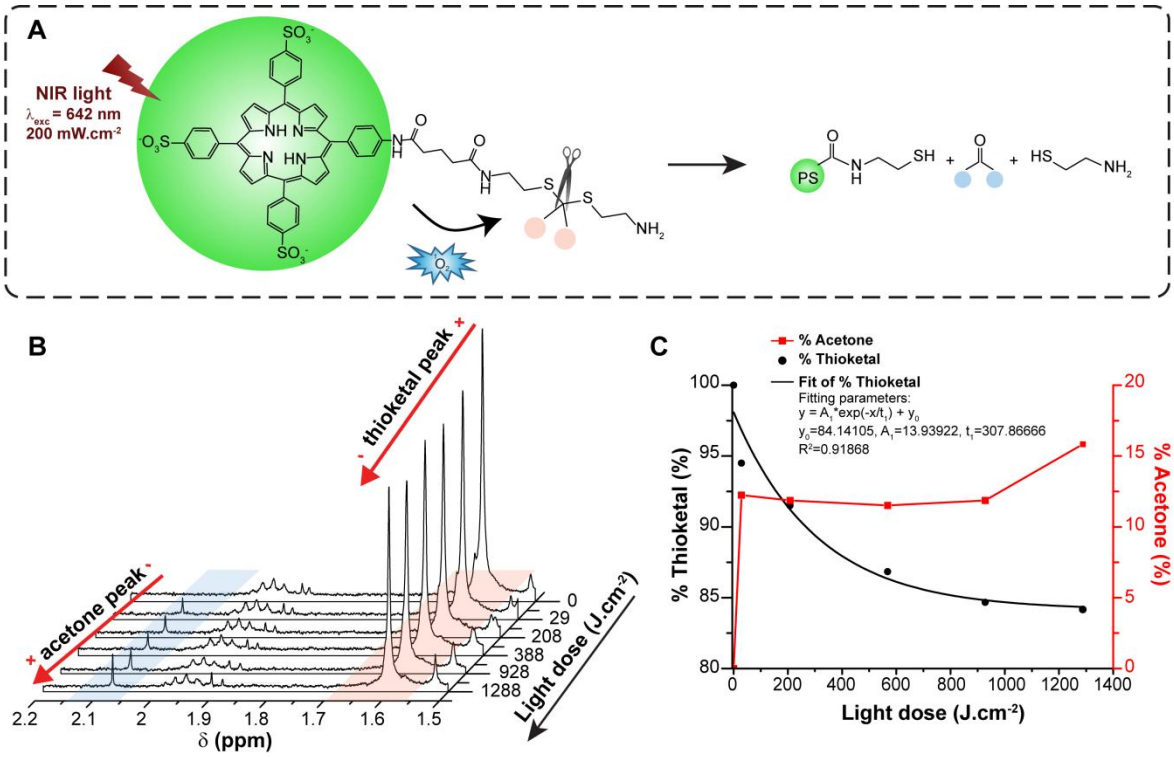

Figure 3. (A) Schematic illustration of the cascaded cleavage of thioketal linker following $TPPS_3$ illumination, **(B)** Partial ^1H NMR spectra (DMSO-d6, 400 MHz) registered during the illumination of a 70 mM $TPPS_3$-TK-NH_2 solution with a 642 nm laser at 200 $mW.cm^{-2}$. **(C)** Percentage of residual thioketal NMR signal (in red, left axis) and of formed acetone NMR signal (in blue, right axis) registered during illumination.

As depicted in **Figures 3B and 3C**, following the first illumination, we observed more decomposition of thioketal groups compared to the subsequent ones. Furthermore, only 16% of thioketal was decomposed even after 2 hours of illumination (fluence up to 1288 $J.cm^{-2}$). This could be explained by several factors related to the experimental conditions. Indeed, added to the low singlet oxygen yield of TPPS porphyrin derivatives in DMSO (example: $\Phi_\Delta(TPPS_4)$ = 0.19 in DMSO [47]), the current experiment was conducted in a closed NMR tube, which limited the renewal of dissolved molecular oxygen during the illumination process thus limiting the production of the oxidative $^1O_2$. In addition, DMSO solvent exhibits higher viscosity compared to water in which the PDA nanoparticles will be suspended, thus the diffusion distance of the singlet oxygen is limited which in turn limits its oxydative efficiency. Moreover, the generation of other reactive species is also expected to be very limited in the DMSO solvent. Knowing that thioketal linkers revealed a higher responsiveness to hydroxyl radical in comparison to other ROS [48], this would further explain the relatively slow cleavage kinetics of thioketal obtained in this study. Finally, it should be noticed that the illuminated NMR tubes contained a high $TPPS_3$-TK-NH_2 concentration which induces the PS aggregation

with subsequent high light scattering. This will limit the penetration depth of light within the tube. The laser diode used for this experiment exhibits a max peak at 642 nm which corresponds to the Q_I band of the PS at which the coefficient extinction is low ($\varepsilon_{642\ nm}$ = 268.5 $M^{-1}.cm^{-1}$) so the number of photons adsorbed by the PS is low when illuminated at this wavelength. Based on the aforementioned and despite the fact that thioketal decomposition was not complete at these illumination conditions, we could demonstrate the cleavage of the TK linker upon the PS illumination. Such decomposition process can be further improved when grafting the PSs at the surface of PDA NPs, where the PSs are not aggregated and will be illuminated with an orange-filtered lamp with a maximum peak at 590 nm where the PS absorbs much more photons as done for the *in vitro* expermients.

3.3. Preparation of the $TPPS_3$-conjugated PDA-PEG NPs

Having calculated the photothermal conversion efficiencies of PDA nanoparticles as function of size, we chose those prepared at a [Ammonia]/[Dopamine] ratio of 25 for further functionalization steps for the design of the bimodal PTT/PDT nanosystem. Since these nanoparticles have a hydrodynamic diameter of ~130 nm and present the best photothermal conversion properties, they should represent a good compromise for future *in vivo* applications.

3.3.1. Synthesis of $TPPS_3$-conjugated PEG polymers

In order to functionalize the PDA nanoparticles with PEG chains that will bear either $TPPS_3$-TK-NH_2 or $TPPS_3$-NH_2 at their extremities, we have used SH-PEG_{2000}-COOH as a bifunctional PEG polymer. Where the thiol group will serve as chemical anchor for the PEG chain on the catechol groups of PDA nanoparticles *via* a Michael addition reaction as demonstrated previously, the carboxylic group can be used for the coupling of the photosensitizers.

Thus, to prepare these multifunctional PDA nanoparticles, we have opted for the following functionalization strategy which is summarized in the **Figure 4**. We first dimerized the SH-PEG_{2000}-COOH polymers into disulfide derivatives to block the thiol groups before their activation and coupling to the porphyrins. Then the carboxylic groups present on both extremities of disulfide PEG polymers were converted into acyl chloride functions. Afterwards, two different porphyrins either $TPPS_3$-TK-NH_2 or $TPPS_3$-NH_2 were conjugated separately on the acyl groups which led to the formation of ROS-responsive and non-ROS responsive polymers respectively. Finally, the disulfides were reduced using TCEP to

regenerate the thiol group which is required for the Michael addition onto the catechol groups of polydopamine.

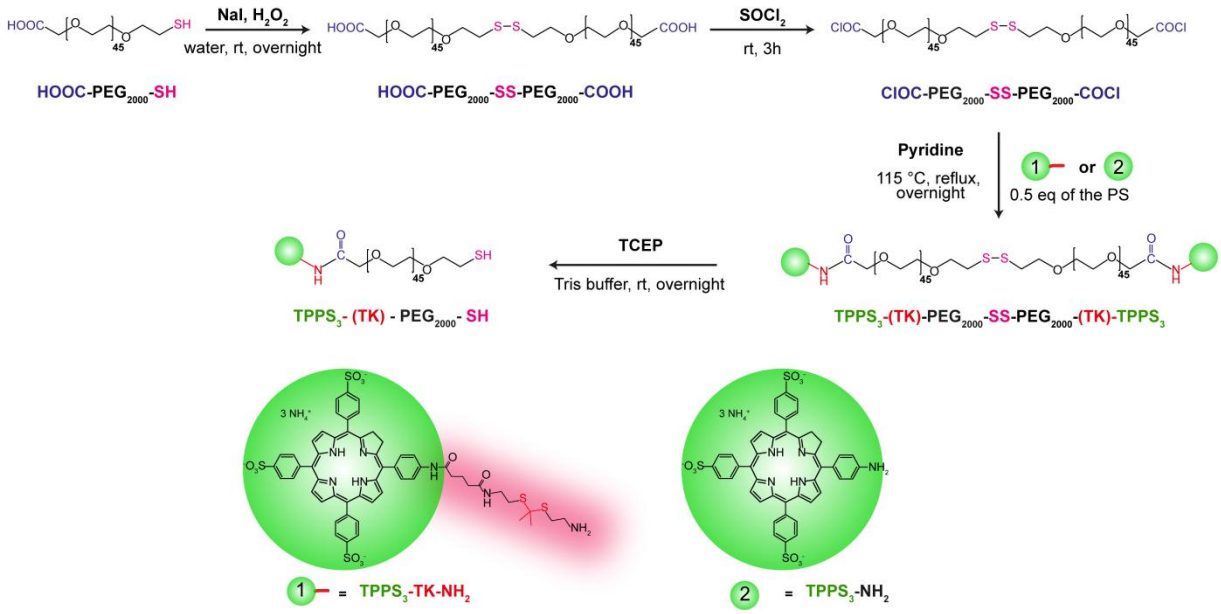

Figure 4. Schematic illustration summarizing the synthesis of $TPPS_3$-(TK)-PEG_{2000}-SH or $TPPS_3$-(NH)-PEG_{2000}-SH polymers.

3.3.2. Assessment of the $TPPS_3$-TK-PEG_{2000}-SH grafting efficiency on PDA film using Quartz Crystal Microbalance with Dissipation monitoring (QCM-D)

Prior to the conjugation of the resulting polymeric complexes to bare PDA NPs, the ability of these chains to be efficiently grafted on PDA surface was first studied on PDA film using QCM-D, as described in a previous work. After the formation of a PDA film on SiO_2 coated quartz, the $TPPS_3$-TK-PEG_{2000}-SH in Tris buffer (10 mM, 150 mM NaCl, pH 8.5) was injected. As depicted in **Figure 5**, a significant decrease of the resonance frequency with subsequent increase in the energy dissipation was observed following this injection. The signals stabilized after 10 hours and remained constant after the buffer rinsing step. This indicates that the $TPPS_3$-TK-PEG_{2000}-SH can be grafted on a PDA adlayer by forming a stable film. In addition, the injection of $TPPS_3$-TK-PEG_{2000}-SH exhibited different grafting kinetics than COOH-PEG_{2000}-SH. The reached values of the frequency shift for $TPPS_3$-TK-PEG_{2000}-SH ($\Delta f_{5=}$ -49 ± 9 Hz, n=3) were similar to those obtained previously [35] with non-conjugated COOH-PEG_{2000}-SH (Δf_5= -49 ± 8 Hz, n=3), thus suggesting that an efficient grafting of the synthesized $TPPS_3$-TK-PEG_{2000}-SH polymers with a high grafting density on the surface of PDA can be achieved in buffer conditions.

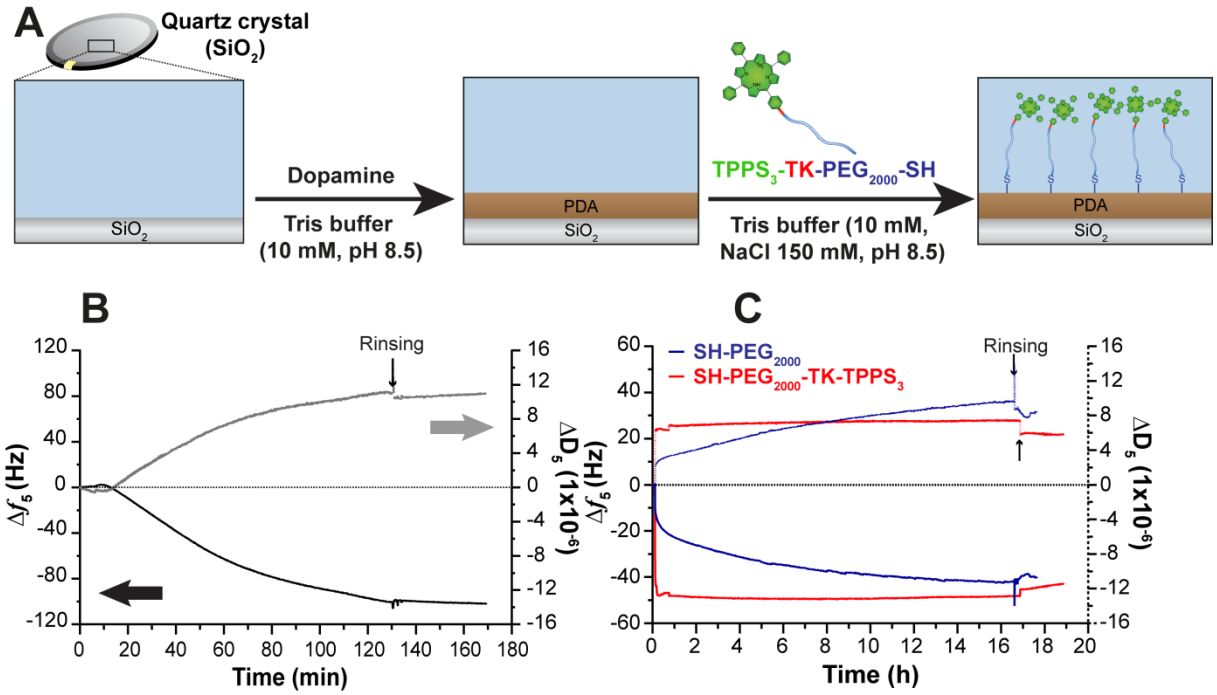

Figure 5. (A) Scheme illustrating the grafting strategy of $TPPS_3$-TK-PEG_{2000}-SH on PDA film using QCM-D. **(B)** Frequency (Δf_5) (black line, left axis) and dissipation (ΔD_5, right axis) (grey line) shifts registered during the formation of a PDA film on a SiO_2 substrates, **(C)** Δf_5 and ΔD_5 obtained following the injection of $TPPS_3$-TK-PEG_{2000}-SH (red curves) on the pre-formed PDA film in Tris buffer (10 mM, 150 mM NaCl, pH 8.5), the results are illustrated in comparison to SH-PEG_{2000}-COOH injected in the same conditions (blue curves).

3.4. Preparation and characterization of PTT/PDT bimodal PDA-based NPs

After demonstrating the capacity of the $TPPS_3$-TK-PEG_{2000}-SH in buffer to be grafted on PDA film, we proceeded with the functionalization of PDA NPs. Hence, PDA NPs of ~130 nm were functionalized in Tris buffer (10 mM, 150 mM NaCl, pH 8.5) using an equal mixture of SH-PEG_{2000}-COOH/$TPPS_3$-(TK)-PEG_{2000}-SH (1:1 mole/mole), in order to avoid a high density of porphyrin on NPs surface that could result in aggregated preparations *in vitro* and unstable systems *in vivo*. Both PDA and PS-conjugated PDA NPs were negatively charged in Tris buffer at pH 7.4 with a zeta-potential of -34±1 mV for bare NPs and -43± 2 mV for the PS-conjugated PDA NPs (**Table 2**). The negative charges could be attributed to the deprotonation of catechol functions exposed at the surface of PDA NPs for the former and to the sulfonate groups of the PS conjugated to NPs surface for the latter. The multifunctional NPs prepared following this approach presented a monodisperse size distribution (**Table 2**).

The efficient PS-PEG grafting on PDA NPs was further assessed by UV-Vis absorption measurements. As depicted in the absorption spectra (**Figure 6**), both ROS-responsive and

non-ROS responsive nanoparticles showed the characteristic absorption peaks of the $TPPS_3$ which demonstrates that the PS conjugated PEG polymers were efficiently bound on the surface of PDA nanoparticles.

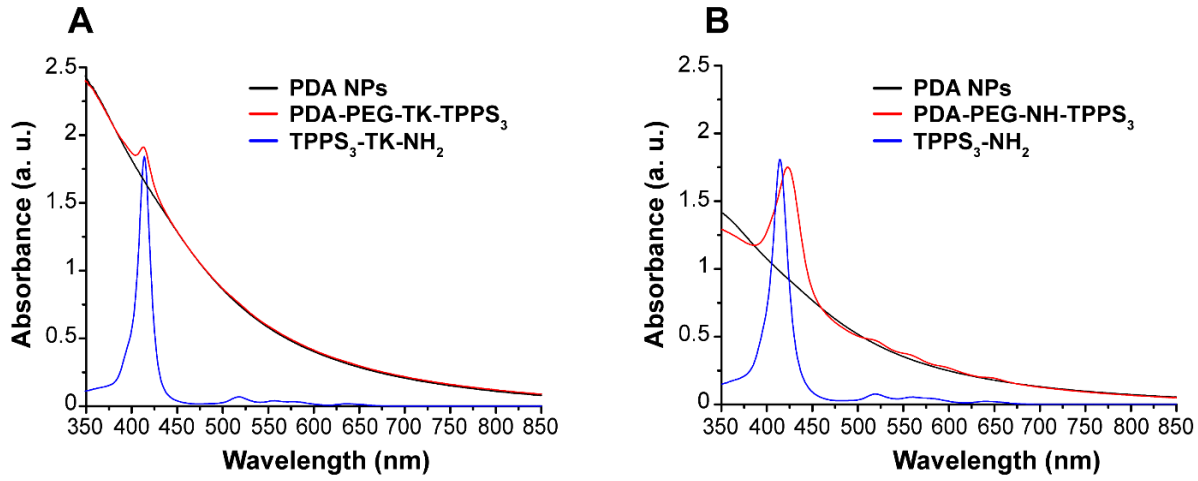

Figure 6: UV-visible absorption spectra of PDA NPs (black lines), ROS-responsive (**A,** red line) or non-ROS responsive (**B,** red line) PS-conjugated PDA NPs, and $TPPS_3$-TK-NH_2 (**A,** blue line) or $TPPS_3$-NH_2 (**B,** blue line), measured in Tris buffer (10 mM, pH 8.5).

After normalization of the absorption spectra PS-conjugated PDA NPs to bare PDA ones, the amounts of $TPPS_3$ photosensitizers attached to the surface of NPs were determined by UV-visible experiments and the molecular ratio PS/NPs was deduced as depicted in (**Table 2**).

Table 2. Summary of the size and zeta-potential values measured by DLS at 25°C for PDA and PS-conjugated PDA NPs, and the molecular ratio of PS to PDA NPs in the full bimodal systems. The reported values are the average ± standard deviation of n = 3.

	Hydrodynamic diameter (nm)	**Zeta-potential (mV)**	**Molecular ratio PS / NPs**
PDA NPs	129 ± 2	-34 ± 1	--
PDA-PEG$_{2000}$-TK-TPPS$_3$	238 ± 4	-43 ± 2	2.4 x 10^5
PDA-PEG$_{2000}$-NH-TPPS$_3$	206 ± 2	-43 ± 2	2.7 x 10^5

3.5. Cell culture experiments

Success in cancer treatment by PDT implies the effective internalization of the PS inside cancerous cells. Thus, in order to evaluate the cell internalization of the PDA-based nanoparticles and to optimize the incubation times of the tested drugs/particles, cellular uptake of the PDA and PDA-PEG NPs and of the free $TPPS_3$-COOH PS was assessed using

flow cytometry (**Figure 7**). The mean fluorescence intensity (MFI) measurements revealed an efficient cellular uptake of the tested NPs and the PS, with uptake observed within the first few hours of incubation. Curiously, in the case of bare PDA NPs, the MFI increased with the incubation time from 30 min to 6 hours following by an abrupt increase in the MFI after 24 hours. This could be explained by the sedimentation of the bare PDA NPs in the culture medium at pH 7.4 as we demonstrated in a previous work [35]. Indeed, PDA NPs can settle with time and remained attached to the cells membrane which induces an overestimation in the MFI values. However, a higher internalization rate of the PEGylated PDA NPs was observed in both HET-1A and KYSE-30 cell lines with saturation in the cell uptake after approximatively 2 h of incubation. This difference in the uptake kinetics demonstrated further the presence of the PEG chains on the surface of PDA NPs. Compared to PDA NPs, the cellular uptake of the free $TPPS_3$ photosensitizer increase monotonically with the incubation time. This implies that the free $TPPS_3$ photosensitizer requires more time than PEGylated PDA NPs to be internalized inside the cells. Thus, PEGylated PDA NPs can be used as efficient nanocarriers of the PS to be internalized faster inside the cells.

To further probe the cellular uptake, experiments were carried out after 24 h of incubation for the PEGylated PDA NPs or for the PS, as it allowed a significant cell internalization and enables optimal evaluation of the cyto/phototoxic effects of the PTT/PDT PDA-based NPs.

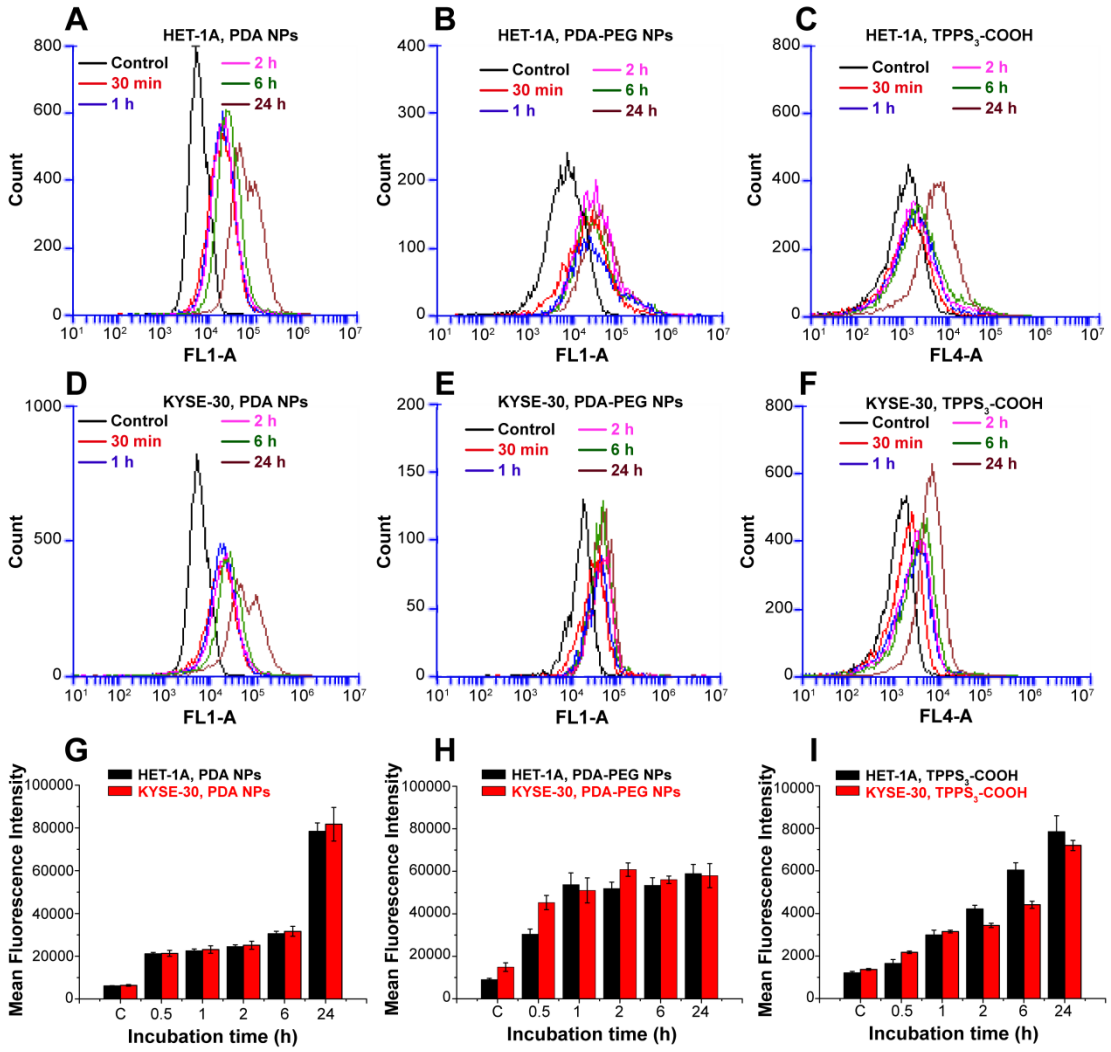

Figure 7. Flow cytometry analysis of the HET-1A and the KYSE-30 cells incubated with FITC-labeled PDA NPs **(A, D)**, with FITC-labeled PDA-PEG NPs **(B, E)**, and with the free $TPPS_3$-COOH photosensitizer **(C,F)**. Mean fluorescence intensities (MFI) obtained after incubation of FITC-labeled PDA NPs **(G)**, FITC-labeled PDA-PEG NPs **(H)** and $TPPS_3$-COOH **(I)** with HET-1A or KYSE-30 cells for different time durations. The error bars correspond to the standard deviation of n = 3.

The non-toxicity or low toxicity in darkness of any photosensitizing agent is a key parameter for any phototherapeutic modality application. Hence, we investigated first the cytotoxicity in darkness of (i) the PDA and PDA-PEG NPs, (ii) the free $TPPS_3$-COOH and (iii) the PDA-PEG_{2000}-TK-$TPPS_3$ or PDA-PEG_{2000}-NH-$TPPS_3$.

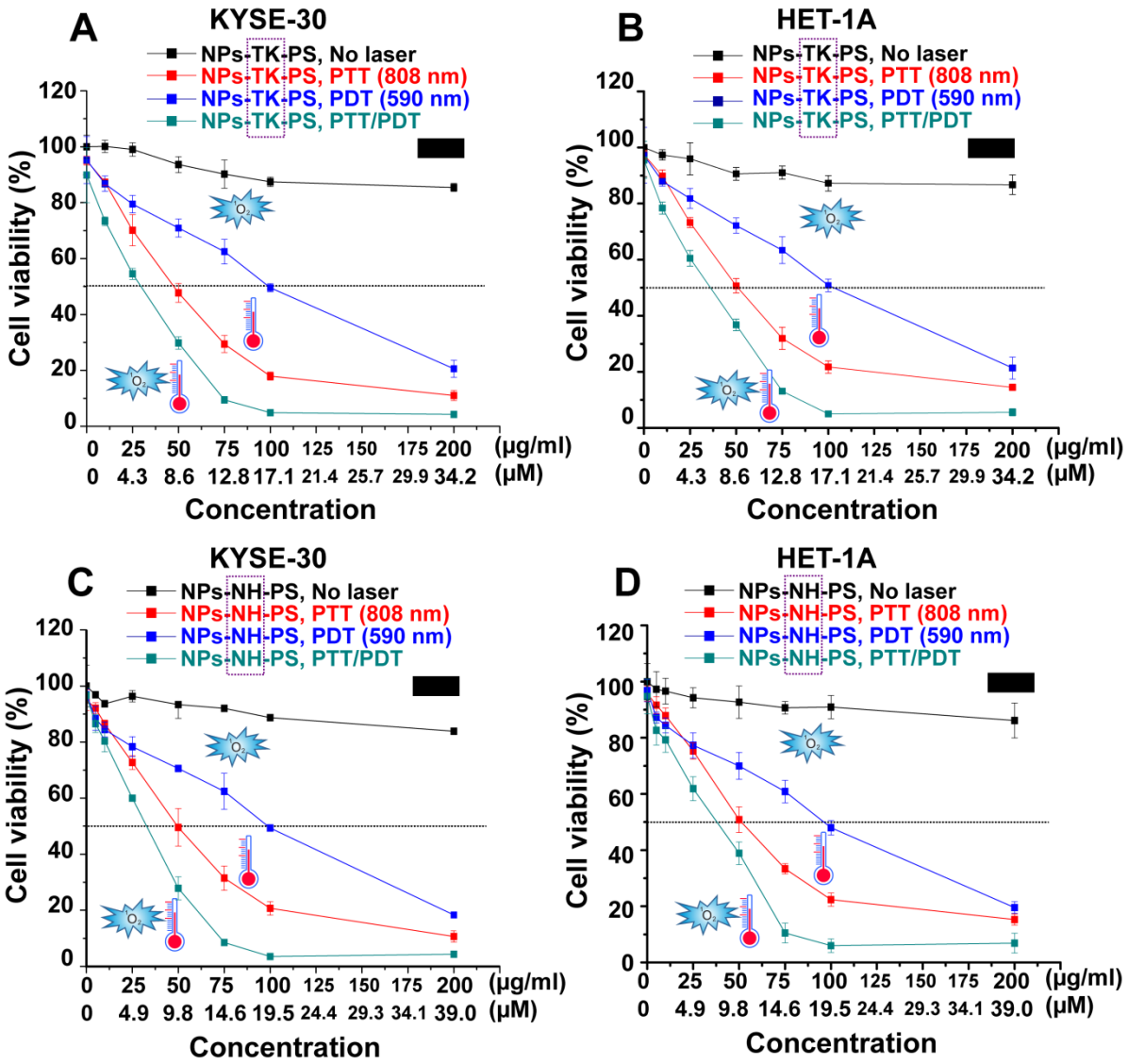

Figure 8. Dose-response curves of the ROS-responsive PDA-based NPs on KYSE-30 (**A**) and HET-1A (**B**) without illumination are presented in black lines, (ii) after PTT illumination (λ_{exc} = 808 nm, 2 W.cm^{-2}, 10 min) in red lines, (iii) after PDT illumination (λ_{max} = 590 nm, 2 J.cm^{-2}) in blue lines and (iv) after PTT/PDT combined illuminations in green lines. **(C)** and **(D)** represent the dose-response curves of the non-ROS responsive PDA-based NPs on KYSE-30 and HET-1A respectively. The concentration of PDA nanoparticles and photosensitizers are expressed in µg/ml and µM respectively. The error bars correspond to the standard deviation of n = 3.

As illustrated in **Figure S7A,** both bare and PEGylated PDA NPs showed a low cytotoxicity after 24 hours over a wide range of concentrations, reaching 500 µg/ml, which confirms their very low toxicity as demonstrated by other authors but in different cancer cell lines [17, 49-51]. As the incubation time of NPs increased from 24 to 72 h, a slight decrease in cell survival percentage was observed (**Figure S8 A-D**), As an example, cell viability decreased from 84%

to 71% for PDA-PEG NPs incubated with HET-1A at 500 µg/ml for 24h and 72h respectively).

Similarly, both cell types maintained high cell viability in presence of free $TPPS_3$-COOH incubated at concentrations up to 60 µM, in the absence of NIR light irradiation (**Figure S7 B-C**). When irradiated with orange filtered lamp at a fluence of 2 $J.cm^{-2}$, we observed a PS dose-dependent phototoxicity, with a half maximal inhibitory concentration (IC_{50}) on KYSE-30 and HET-1A of 32.0 ± 1.0 and 35.0 ± 1.0 µM, respectively (**Figure S7 C**, **Table 3**). In agreement with this result, PDT IC_{50} ranging between low µM and tens of µM were reported in the literature for sulfonated tetraphenyl porphyrins depending on the irradiation conditions and the cell type [52-54]. Such relatively high values are most likely related to relatively low singlet oxygen quantum yields and/or to a low cellular internalization due to their hydrophilic character [52].

Afterwards, the PDT and/or PTT effects of the ROS-responsive PDA-based NPs were then assessed and compared to that of the non-ROS responsive nanosystem used as control, *i.e.*, the $TPPS_3$-NH-PEG-PDA NPs. As illustrated in **Figure 8A-D**, the functionalized PDA NPs showed a dose-dependent PTT effect after laser irradiation (808 nm, 2 $W.cm^{-2}$) for 10 min, leading to the killing of more than 85% of cells at 200 µg/ml of PDA. This effect was attributed to the increasing heat generation observed in cells incubated as PDA concentrations increased. The infrared images recorded following PTT illuminations are presented in **Figure S9** and confirmed the increase of temperature in each well upon illumination. Similar PTT effects were obtained on both cell types.

Under PDT illumination conditions, cell viability decreased to almost 20% for a PS concentration equivalent to 34.2 µM for $TPPS_3$-TK-NH_2 and ~39.0 µM for $TPPS_3$-NH_2 (**Figure 8 A-D**). Similar results were obtained for both cell types. The IC_{50} after PDT illumination conditions was found to be of 16.9 µM and 19.3 µM for the ROS-responsive and non-ROS responsive nanoplatforms, respectively, which is much lower than that obtained for the free $TPPS_3$-COOH. This significant enhancement in the PS phototoxicity is more likely related to an improved solubility in the culture medium and/or a higher cell internalization of the PS when it is attached to the surface of NPs as deduced from the flow cytometry experiments.

Interestingly, the combination of PDT and PTT NIR light illuminations resulted in a dramatic decrease of cell viability, as shown in **Figures 8** and **9**. Indeed, at a PDA concentration of 200 µg/ml ($TPPS_3$-TK-NH_2 and $TPPS_3$-NH_2 concentrations equivalent to 34.2 µM and 39.0 µM

respectively), more than 95% of cells were killed, which demonstrates the great potential of these bimodal nanoplatforms in eradicating cancer cells.

To identify the nature of the phototherapeutic combination effect, the combination indexes (CI) were calculated according to Chou-Talalay formalism. CI below 1 indicates a synergy, CI = 1 accounts for additive effects and CI > 1 for drug antagonism. The CI values listed in **Table 3** were below 0.3 accounting for a strong synergistic effect of combining PTT and PDT in single nanoplatform [55].

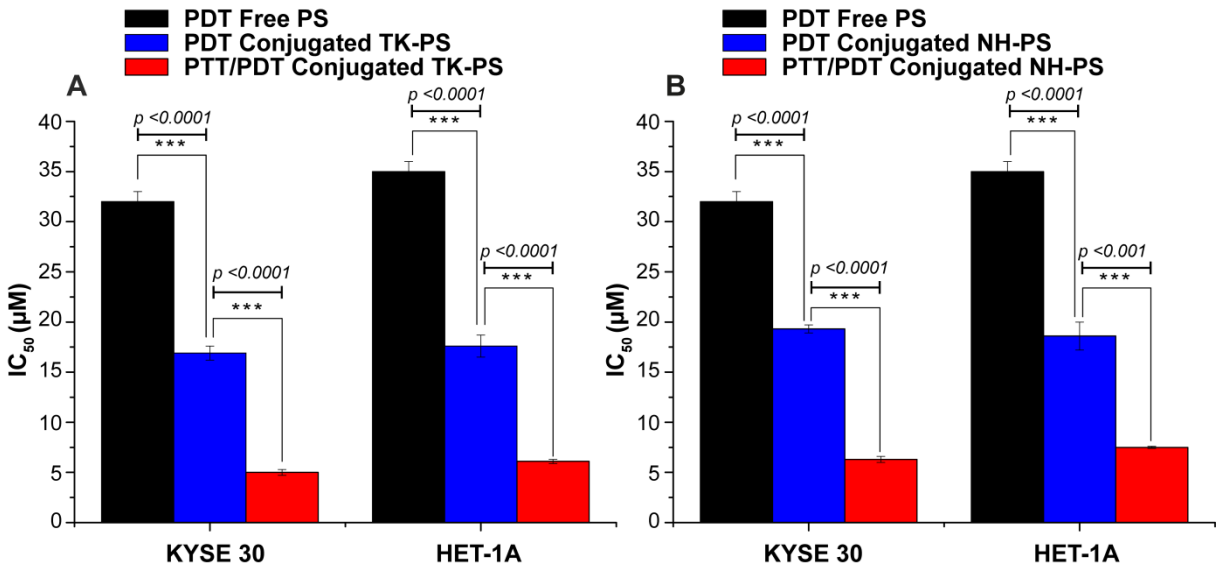

Figure 9. Histograms of IC_{50} values in KYSE-30 and HET-1A cell lines (n=3) after PDT treatment with the free photosensitizer (black) and after PDT (blue) or PTT/PDT (red) with the ROS-responsive **(A)** or non-ROS responsive **(B)** PS-conjugated PDA NPs,

In addition, ROS-responsive PDA NPs showed a better photodynamic effect compared to the non-ROS responsive NPs on both cell lines, with a slight difference in the IC_{50} values between them as shown in **Figure 9** and **Table 3**. Interestingly, such difference in IC_{50} between the two nanoplatforms is significant as determined by the unpaired two sample Student's t-test ($P<0.007$ for KYSE-30 cell line and $P<0.005$ for HET-1A cell line). The small decrease in IC_{50} of the ROS-responsive PDA-based NPs compared to non-ROS responsive ones could be related to the illumination conditions. Indeed, the light dose used in the phototoxicity tests may be insufficient to induce complete thioketal decomposition with subsequent PS migration to ROS-sensitive organelles where it would exert an optimal photodynamic effect *in situ*.

Table 3. Photothermal and/or photodynamic toxicities, of the ROS-responsive or non-sensitive nanosystems on KYSE-30 and HET-1A cell lines under separate or combined NIR irradiations (PTT and/or PDT), related to PDA NPs (IC_{50}, µg/ml) and $TPPS_3$ (IC_{50}, µM) respectively. CI is their combination index. The reported values are the average ± standard deviation of n =3.

		PDA-PEG-TK-$TPPS_3$		**PDA-PEG-NH-$TPPS_3$**	
		KYSE-30	**HET-1A**	**KYSE-30**	**HET-1A**
PTT/PDT	**CI**	0.25	0.28	0.25	0.27
	PS (IC_{50}, µM)	5.0 ± 0.3	6.1 ± 0.2	6.3 ± 0.3	7.5 ± 0.1
	PDA (IC_{50}, µg/ml)	29.2 ± 1.6	35.5 ± 1.3	32.5 ± 1.5	38.3 ± 0.6
PTT alone	**PS (IC_{50}, µM)**	--	--	--	--
	PDA (IC_{50}, µg/ml)	47.2 ± 4.1	51.2 ± 3.3	49.2 ± 6.8	51.3 ± 4.6
PDT alone	**PS (IC_{50}, µM)**	16.9 ± 0.7	17.6 ± 1.1	19.3 ± 0.4	18.6 ± 1.4
	PDA (IC_{50}, µg/ml)	--	--	--	--

CONCLUSION

In this work, bimodal PTT/PDT PDA NPs were successfully prepared and characterized. They were PEGylated and conjugated to a $TPPS_3$ photosensitizer coupled directly to the PEG extremity or *via* a ROS-responsive linker (i.e., thioketal). The photo-triggered release of the PS upon the cleavage of the thioketal linker could be demonstrated *in vitro.* These nanoplatforms showed a very low dark cytotoxicity *in vitro* but exhibited high photothermal conversion efficiency with higher photodynamic effect on esophageal cancer cell lines compared to the free PS. In addition, the ROS-responsive PDA NPs showed a higher PDT efficiency compared to non-ROS responsive ones. Interestingly, a synergistic phototoxic effect in vitro was obtained in vitro by combining both phototherapeutic modalities following the illumination at two different wavelengths. Taken together, this work demonstrated the high potential of PDA-based nanoconstructs for bimodal PTT/PDT of cancer with controlled release functionality of the PS upon demand.

ASSOCIATED CONTENT

Supporting Information

(1) Scheme of the experimental setup adopted for the photothermal conversion efficiency determination. (2) Photothermal conversion efficiency calculation. (3) NMR characterization of COOH-PEG_{2000}-S-S-PEG_{2000}-COOH and COOH-PEG2000-SH compounds. (4) NMR characterization of $TPPS_3$-TK-PEG_{2000}-SH and $TPPS_3$-NH-PEG_{2000}-SH conjugates. (5) Standard curves of absorbance versus concentration of the photosensitizers in Tris buffer. (6) Photothermal conversion percentage efficiency of PDA nanoparticles in Tris buffer (10 mM, pH 8.5) as function of their hydrodynamic diameter. (7) Cell viability of HET-1A and KYSE-30 cells treated with different concentrations of PDA NPs, PDA-PEG NPs or$TPPS_3$-COOH with or without laser illumination. (8) Cell viability of KYSE-30 and HET-1A cells treated with different concentrations of PDA NPs, PDA-PEG NPs or$TPPS_3$-COOH with or without laser illumination after 24h, 48h and 72h of treatment. (9) Infrared thermal images and the temperature increase (ΔT) registered after PTT laser treatment of the cell lines.

This material is available free of charge via the Internet at http://pubs.acs.org.

ACKNOWLEDGMENTS

IZ is thankful to the French Ministry of Research for the financial support of her PhD thesis. IZ is also thankful to Dr Antonio Lipa Castro for his help on cell cultures. The financial supports for PDT and PTT research from the ANR JCJC Grant (Project-ANR-19-CE09-0015), from MITI Auto-organisation 2021 and from the Laboratory of Excellence LERMIT via an ANR grant (ANR-10-LABX-33) under the program of ‘‘Investissements d’avenir’’ are gratefully acknowledged. We also acknowledge PorphyChem for the fruitful discussion about the porphyrin conjugation protocol.

References

1. Li, X.; Lovell, J. F.; Yoon, J.; Chen, X. Clinical development and potential of photothermal and photodynamic therapies for cancer. *Nature Reviews Clinical Oncology* **2020,** *17*, (11), 657-674.
2. Silva, P. D.; Saad, M. A.; Thomsen, H. C.; Bano, S.; Ashraf, S.; Hasan, T. Photodynamic therapy, priming and optical imaging: Potential co-conspirators in treatment design and optimization — a Thomas Dougherty Award for Excellence in PDT paper. *Journal of Porphyrins and Phthalocyanines* **2020,** *24*, (11n12), 1320-1360.
3. Zmerli, I.; Michel, J.-P.; Makky, A. Multifunctional polydopamine-based nanoparticles: synthesis, physico-chemical properties and applications for bimodal photothermal/photodynamic therapy of cancer. *Multifunctional Materials* **2021,** *4*, (2), 022001.
4. Zhou, L.; Chen, L.; Hu, X.; Lu, Y.; Liu, W.; Sun, Y.; Yao, T.; Dong, C.; Shi, S. A Cu9S5 nanoparticle-based CpG delivery system for synergistic photothermal-, photodynamic- and immunotherapy. *Communications Biology* **2020,** *3*, (1), 343.

5. Lin, J.; Wang, S.; Huang, P.; Wang, Z.; Chen, S.; Niu, G.; Li, W.; He, J.; Cui, D.; Lu, G.; Chen, X.; Nie, Z. Photosensitizer-Loaded Gold Vesicles with Strong Plasmonic Coupling Effect for Imaging-Guided Photothermal/Photodynamic Therapy. *ACS Nano* **2013,** *7*, (6), 5320-5329.
6. Jang, B.; Park, J.-Y.; Tung, C.-H.; Kim, I.-H.; Choi, Y. Gold Nanorod−Photosensitizer Complex for Near-Infrared Fluorescence Imaging and Photodynamic/Photothermal Therapy In Vivo. *ACS Nano* **2011,** *5*, (2), 1086-1094.
7. Vankayala, R.; Lin, C.-C.; Kalluru, P.; Chiang, C.-S.; Hwang, K. C. Gold nanoshells-mediated bimodal photodynamic and photothermal cancer treatment using ultra-low doses of near infra-red light. *Biomaterials* **2014,** *35*, (21), 5527-5538.
8. Sun, J.; Guo, Y.; Xing, R.; Jiao, T.; Zou, Q.; Yan, X. Synergistic in vivo photodynamic and photothermal antitumor therapy based on collagen-gold hybrid hydrogels with inclusion of photosensitive drugs. *Colloids and Surfaces A: Physicochemical and Engineering Aspects* **2017,** *514*, 155-160.
9. Chambre, L.; Saw, W. S.; Ekineker, G.; Kiew, L. V.; Chong, W. Y.; Lee, H. B.; Chung, L. Y.; Bretonnière, Y.; Dumoulin, F.; Sanyal, A. Surfactant-Free Direct Access to Porphyrin-Cross-Linked Nanogels for Photodynamic and Photothermal Therapy. *Bioconjugate Chem* **2018,** *29*, (12), 4149-4159.
10. Han, J.; Park, W.; Park, S.-j.; Na, K. Photosensitizer-Conjugated Hyaluronic Acid-Shielded Polydopamine Nanoparticles for Targeted Photomediated Tumor Therapy. *Acs Appl Mater Inter* **2016,** *8*, (12), 7739-7747.
11. Xing, Y.; Ding, T.; Wang, Z.; Wang, L.; Guan, H.; Tang, J.; Mo, D.; Zhang, J. Temporally Controlled Photothermal/Photodynamic and Combined Therapy for Overcoming Multidrug Resistance of Cancer by Polydopamine Nanoclustered Micelles. *Acs Appl Mater Inter* **2019,** *11*, (15), 13945-13953.
12. Liu, L.-H.; Qiu, W.-X.; Li, B.; Zhang, C.; Sun, L.-F.; Wan, S.-S.; Rong, L.; Zhang, X.-Z. A Red Light Activatable Multifunctional Prodrug for Image-Guided Photodynamic Therapy and Cascaded Chemotherapy. *Advanced Functional Materials* **2016,** *26*, (34), 6257-6269.
13. Yuan, Y.; Liu, J.; Liu, B. Conjugated-Polyelectrolyte-Based Polyprodrug: Targeted and Image-Guided Photodynamic and Chemotherapy with On-Demand Drug Release upon Irradiation with a Single Light Source. *Angewandte Chemie International Edition* **2014,** *53*, (28), 7163-7168.
14. Yue, C.; Zhang, C.; Alfranca Ramón, G.; Yang, Y.; Jiang, X.; Yang, Y.; Pan, F.; Fuente, J.; Cui, D. Near-Infrared Light Triggered ROS-activated Theranostic Platform based on Ce6-CPT-UCNPs for Simultaneous Fluorescence Imaging and Chemo-Photodynamic Combined Therapy. *Theranostics* **2016,** *6*, 456-469.
15. Han, K.; Zhu, J.-Y.; Wang, S.-B.; Li, Z.-H.; Cheng, S.-X.; Zhang, X.-Z. Tumor targeted gold nanoparticles for FRET-based tumor imaging and light responsive on-demand drug release. *Journal of Materials Chemistry B* **2015,** *3*, (41), 8065-8069.
16. Zmerli, I.; Michel, J.-P.; Makky, A. Bioinspired polydopamine nanoparticles: synthesis, nanomechanical properties, and efficient PEGylation strategy. *Journal of Materials Chemistry B* **2020,** *8*, (20), 4489-4504.
17. Liu, Y.; Ai, K.; Liu, J.; Deng, M.; He, Y.; Lu, L. Dopamine-Melanin Colloidal Nanospheres: An Efficient Near-Infrared Photothermal Therapeutic Agent for In Vivo Cancer Therapy. *Advanced Materials* **2013,** *25*, (9), 1353-1359.
18. Liu, Y.; Ai, K.; Lu, L. Polydopamine and Its Derivative Materials: Synthesis and Promising Applications in Energy, Environmental, and Biomedical Fields. *Chemical Reviews* **2014,** *114*, (9), 5057-5115.
19. Liu, H.; qu, X.; Tan, H.; Song, J.; Lei, M.; Kim, E.; Payne, G.; Liu, C. Role of Polydopamine's Redox-Activity on its Pro-oxidant, Radical-Scavenging, and Antimicrobial Activities. *Acta Biomaterialia* **2019,** *88*.
20. Hu, J.; Yang, L.; Yang, P.; Jiang, S.; Liu, X.; Li, Y. Polydopamine free radical scavengers. *Biomaterials Science* **2020,** *8*, (18), 4940-4950.
21. Liu, Y.; Ai, K.; Ji, X.; Askhatova, D.; Du, R.; Lu, L.; Shi, J. Comprehensive Insights into the Multi-Antioxidative Mechanisms of Melanin Nanoparticles and Their Application To Protect Brain from Injury in Ischemic Stroke. *Journal of the American Chemical Society* **2017,** *139*, (2), 856-862.

22. Liu, H.; Yang, Y.; Liu, Y.; Pan, J.; Wang, J.; Man, F.; Zhang, W.; Liu, G. Melanin-Like Nanomaterials for Advanced Biomedical Applications: A Versatile Platform with Extraordinary Promise. *Advanced Science* **2020,** *7*, (7), 1903129.
23. Yang, P.; Gu, Z.; Zhu, F.; Li, Y. Structural and Functional Tailoring of Melanin-Like Polydopamine Radical Scavengers. *CCS Chemistry* **2020,** *2*, (2), 128-138.
24. Richardson, H. H.; Carlson, M. T.; Tandler, P. J.; Hernandez, P.; Govorov, A. O. Experimental and Theoretical Studies of Light-to-Heat Conversion and Collective Heating Effects in Metal Nanoparticle Solutions. *Nano Letters* **2009,** *9*, (3), 1139-1146.
25. Roper, D. K.; Ahn, W.; Hoepfner, M. Microscale Heat Transfer Transduced by Surface Plasmon Resonant Gold Nanoparticles. *The Journal of Physical Chemistry C* **2007,** *111*, (9), 3636-3641.
26. Jiang, K.; Smith, D. A.; Pinchuk, A. Size-Dependent Photothermal Conversion Efficiencies of Plasmonically Heated Gold Nanoparticles. *The Journal of Physical Chemistry C* **2013,** *117*, (51), 27073-27080.
27. Cantu, T.; Walsh, K.; Moy, A.; Tunnell, J.; Irvin, J.; Betancourt, T.; Pattani, V. Conductive polymer-based nanoparticles for laser-mediated photothermal ablation of cancer: Synthesis, characterization, and in vitro evaluation. *International Journal of Nanomedicine* **2017,** *12*, 615-632.
28. Pattani, V. P.; Tunnell, J. W. Nanoparticle-mediated photothermal therapy: A comparative study of heating for different particle types. *Lasers in Surgery and Medicine* **2012,** *44*, (8), 675-684.
29. Chen, H.; Shao, L.; Ming, T.; Sun, Z.; Zhao, C.; Yang, B.; Wang, J. Understanding the Photothermal Conversion Efficiency of Gold Nanocrystals. *Small* **2010,** *6*, (20), 2272-2280.
30. Ge, R.; Lin, M.; Li, X.; Liu, S.; Wang, W.; Li, S.; Zhang, X.; Liu, Y.; Liu, L.; Shi, F.; Sun, H.; Zhang, H.; Yang, B. Cu2+-Loaded Polydopamine Nanoparticles for Magnetic Resonance Imaging-Guided pH- and Near-Infrared-Light-Stimulated Thermochemotherapy. *ACS Applied Materials & Interfaces* **2017,** *9*, (23), 19706-19716.
31. Ling, X.; Zhang, S.; Shao, P.; Wang, P.; Ma, X.; Bai, M. Synthesis of a reactive oxygen species responsive heterobifunctional thioketal linker. *Tetrahedron letters* **2015,** *56*, 5242-5244.
32. Nieto, C.; Vega, M. A.; Marcelo, G.; Martín del Valle, Eva M. Polydopamine nanoparticles kill cancer cells. *RSC Advances* **2018,** *8*, (63), 36201-36208.
33. Chou, T.-C. Drug Combination Studies and Their Synergy Quantification Using the Chou-Talalay Method. *Cancer research* **2010,** *70*, 440-6.
34. Chou, T.-C.; Talalay, P. Quantitative Analysis of Dose-Effect Relationships: The Combined Effects of Multiple Drugs or Enzyme Inhibitors. *Advances in enzyme regulation* **1984,** *22*, 27-55.
35. Zmerli, I.; Michel, J.-P.; Makky, A. Bioinspired polydopamine nanoparticles: synthesis, nanomechanical properties, and efficient PEGylation strategy. *Journal of Materials Chemistry B* **2020**.
36. Liebscher, J. Chemistry of Polydopamine – Scope, Variation, and Limitation. *European Journal of Organic Chemistry* **2019,** *2019*, (31-32), 4976-4994.
37. Della Vecchia, N. F.; Avolio, R.; Alfè, M.; Errico, M. E.; Napolitano, A.; d'Ischia, M. Building-Block Diversity in Polydopamine Underpins a Multifunctional Eumelanin-Type Platform Tunable Through a Quinone Control Point. *Advanced Functional Materials* **2013,** *23*, (10), 1331-1340.
38. Ball, V. Polydopamine Nanomaterials: Recent Advances in Synthesis Methods and Applications. *Front Bioeng Biotechnol* **2018,** *6*, 109.
39. Noguchi, Y.; Wu, J.; Duncan, R.; Strohalm, J.; Ulbrich, K.; Akaike, T.; Maeda, H. Early Phase Tumor Accumulation of Macromolecules: A Great Difference in Clearance Rate between Tumor and Normal Tissues. *Japanese Journal of Cancer Research* **1998,** *89*, (3), 307-314.
40. Singh, R.; Lillard, J. W. Nanoparticle-based targeted drug delivery. *Experimental and Molecular Pathology* **2009,** *86*, (3), 215-223.
41. Liu, X.; Shan, G.; Yu, J.; Yang, W.; Ren, Z.; Wang, X.; Xie, X.; Chen, H.-j.; Chen, X. Laser heating of metallic nanoparticles for photothermal ablation applications. *AIP Advances* **2017,** *7*, (2), 025308.
42. Skrabalak, S. E.; Chen, J.; Sun, Y.; Lu, X.; Au, L.; Cobley, C. M.; Xia, Y. Gold Nanocages: Synthesis, Properties, and Applications. *Accounts of Chemical Research* **2008,** *41*, (12), 1587-1595.
43. Ding, X.; Liow, C. H.; Zhang, M.; Huang, R.; Li, C.; Shen, H.; Liu, M.; Zou, Y.; Gao, N.; Zhang, Z.; Li, Y.; Wang, Q.; Li, S.; Jiang, J. Surface Plasmon Resonance Enhanced Light Absorption

and Photothermal Therapy in the Second Near-Infrared Window. *Journal of the American Chemical Society* **2014,** *136*, (44), 15684-15693.
44. Wang, Y.; Black, K. C. L.; Luehmann, H.; Li, W.; Zhang, Y.; Cai, X.; Wan, D.; Liu, S.-Y.; Li, M.; Kim, P.; Li, Z.-Y.; Wang, L. V.; Liu, Y.; Xia, Y. Comparison Study of Gold Nanohexapods, Nanorods, and Nanocages for Photothermal Cancer Treatment. *ACS Nano* **2013,** *7*, (3), 2068-2077.
45. Mie, G. Beiträge zur Optik trüber Medien, speziell kolloidaler Metallösungen. *Annalen der Physik* **1908,** *330*, (3), 377-445.
46. Horvath, H. Gustav Mie and the scattering and absorption of light by particles: Historic developments and basics. *Journal of Quantitative Spectroscopy and Radiative Transfer* **2009,** *110*, (11), 787-799.
47. Ndube-Tsolekile, N.; Vuyelwa, N.; Obiyenwa, G.; Matoetoe, M.; Songca, S.; Oluwafemi, O. Synthesis of meso-tetra-(4-sulfonatophenyl) porphyrin (TPPS4) – CuInS/ZnS quantum dots conjugate as an improved photosensitizer. *International Journal of Nanomedicine* **2019,** *Volume 14*, 7065-7078.
48. Xu, Q.; He, C.; Xiao, C.; Chen, X. Reactive Oxygen Species (ROS) Responsive Polymers for Biomedical Applications. *Macromolecular Bioscience* **2016,** *16*, (5), 635-646.
49. Gao, Y.; Wu, X.; Zhou, L.; Su, Y.; Dong, C. M. A sweet polydopamine nanoplatform for synergistic combination of targeted chemo-photothermal therapy. *Macromolecular rapid communications* **2015,** *36*, (10), 916-22.
50. Yu, X.; Tang, X.; He, J.; Yi, X.; Xu, G.; Tian, L.; Zhou, R.; Zhang, C.; Yang, K. Polydopamine Nanoparticle as a Multifunctional Nanocarrier for Combined Radiophotodynamic Therapy of Cancer. *Particle & Particle Systems Characterization* **2017,** *34*, (2), 1600296.
51. Zhu, Z.; Su, M. Polydopamine Nanoparticles for Combined Chemo- and Photothermal Cancer Therapy. *Nanomaterials (Basel, Switzerland)* **2017,** *7*, (7).
52. Tita, S. P. S.; Perussi, J. R. The effect of porphyrins on normal and transformed mouse cell lines in the presence of visible light. *Brazilian Journal of Medical and Biological Research* **2001,** *34*, 1331-1336.
53. Kolarova, H.; Nevrelova, P.; Tomankova, K.; Kolar, P.; Bajgar, R.; Mosinger, J. Production of reactive oxygen species after photodynamic therapy by porphyrin sensitizers. *General physiology and biophysics* **2008,** *27*, 101-5.
54. Malina, L.; Tomankova, K. B.; Malohlava, J.; Jiravova, J.; Manisova, B.; Zapletalova, J.; Kolarova, H. The in vitro cytotoxicity of metal-complexes of porphyrin sensitizer intended for photodynamic therapy. *Toxicology in Vitro* **2016,** *34*, 246-256.
55. Chou, T. The mass-action law based algorithm for cost-effective approach for cancer drug discovery and development. *American journal of cancer research* **2011,** *1 7*, 925-54.